Invited Feature Article

Thermal diffusion in binary mixtures: transient behavior and transport coefficients from equilibrium and non-equilibrium molecular dynamics

Sara Bonella, Mauro Ferrario, and Giovanni Ciccotti

Langmuir, **Just Accepted Manuscript** • DOI: 10.1021/acs.langmuir.7b02565 • Publication Date (Web): 15 Sep 2017

Thermal diffusion in binary mixtures: transient behavior and transport coefficients from equilibrium and non-equilibrium molecular dynamics

Sara Bonella,*,† Mauro Ferrario,‡ and Giovanni Ciccotti¶,§,‖

†*CECAM Centre Européen de Calcul Atomique et Moléculaire, École Polytechnique Fédérale de Lausanne, Batochime, Avenue Forel 2, 1015 Lausanne, Switzerland*

‡*Dipartimento di Scienze Fisiche, Informatiche e Matematiche, University of Modena and Reggio Emilia, Via Campi 213/A , 41125 Modena, Italy*

¶*Institute for Applied Mathematics "Mauro Picone" (IAC), CNR, Via dei Taurini 19, 00185 Rome, Italy*

§*University of Rome "La Sapienza", P.le Aldo Moro 5, 00185 Rome, Italy*

‖*University College Dublin (UCD), Belfield, Dublin 4, Ireland*

E-mail: sara.bonella@epfl.ch

Abstract

Equilibrium and non-equilibrium molecular dynamics simulations are combined to compute the full set of coefficients that appear in the phenomenological equations describing thermal transport in a binary mixture subject to a constant thermal gradient. The Dynamical Non-Equilibrium Molecular Dynamics approach (D-NEMD) is employed to obtain the microscopic time evolution of the density and temperature fields, together with that of the mass and energy fluxes. D-NEMD enables to study

not only the steady state, but also the evolution of the fields during the transient that follows the onset of the thermal gradient, up to the establishment of the steady state. This makes it possible to ensure that the system has indeed reached a stationary condition, and to analyze the transient mechanisms and time scales of the mass and energy transport. A local time averaging procedure is applied to each trajectory contributing to the calculation to improve the signal to noise ratio in the estimation of the fluxes and to obtain a clear signal with the, relatively limited, statistics available.

Introduction

Thermal transport in simple dense fluids is an interesting phenomenon whose description in the framework of classical statistical mechanics has been elegantly reviewed, in particular, in a vintage chapter by K. E. Gubbins[1]. In this paper, we shall focus on the coupled mass and energy diffusion in a binary mixture subject to a constant thermal gradient and consider the evaluation of the thermal transport coefficients via computer simulation. It is well known[2–4] that a system subjected to a constant thermal gradient will be driven to a non-equilibrium steady state such that energy (heat) flows at a constant rate through it, while the mass flux stops and a constant concentration gradient is established. This thermal diffusion process, known as the Ludwig-Soret effect, was first observed in 1856 in sulfur-solfate solutions and has since been identified experimentally in a broad range of systems, ranging from gases to polymer mixtures[5–7]. The experimental characterization of the Ludwig-Soret effect is, however, challenging[8]. In mutual diffusion, in fact, thermally driven flows are considerably smaller than, for example, density driven flows and therefore difficult to measure accurately. Molecular Dynamics (MD) based simulations have then been used[4,9–21], together with purely theoretical work, to investigate thermal transport and compute, in particular, the Soret coefficient. Important technical issues, such as the proper definition of the microscopic estimator for the heat flux, have been clarified by these calculations[12], but they are limited to the steady state. As discussed more in detail in the

following, the approach that we employ, the D-NEMD method[22], makes it possible to study also the onset of the transport phenomena and the evolution of hydrodynamic fields towards the steady state, if the latter exists. We shall exploit this feature to study the Ludwig-Soret effect focusing at first on the transient response of the system as described by the relaxation of the time dependent number and temperature density fields and the mass and energy currents. Following this relaxation in time, the transient transport mechanisms and the time scales for the different fluxes will be investigated in some detail. Calculations in the steady state will then be combined with the evaluation, from the time autocorrelation function of the mass current at equilibrium, of the mutual diffusion coefficient to compute the Onsager thermal transport coefficients[23,24] that characterize the Ludwig-Soret effect.

The paper is organized as follows. We begin by summarizing the key phenomenological equations, indicating the relevant transport coefficients and how they will be calculated from simulations. This is followed by a description of the D-NEMD approach and the definition of the estimators for the microscopic fields and fluxes studied. A smoothing scheme adopted to reduce the noise on the estimated currents is also discussed. We conclude the Methods and Model section providing details on the adopted model (an equimolar mixture of Lennard-Jones Argon and Krypton) and on the set-up chosen to simulate the constant thermal gradient. Results are then discussed, followed by some conclusions.

Methods and Model

Macroscopic model and relevant coefficients

To set the stage and introduce some notation, let us recall that the key fields for describing thermal diffusion in a binary mixture are $\mathbf{J}_e$, the energy current density, and $\mathbf{J}_1$ the diffusion current density of species 1 relative to the center of mass frame of reference. For a binary mixture $\mathbf{J}_2 = -\mathbf{J}_1$, where the subscripts $1, 2$ are the indexes of the species. In the following 1 will refer to Kr and 2 to Ar. Adopting a hydrodynamic point of view, the divergence

of the energy current and species diffusion current drives the time evolution of the energy and species mass density fields, respectively (the other continuity equations relating the time derivatives of the total mass density to the divergence of the total momentum, and the time derivative of the momentum density to the divergence of the stress tensor are not relevant in this work). In 1971, Trimble and Deutch[25], derived the linearized hydrodynamic equations for a two-component mixture starting from a microscopic description based on Kubo's linear response theory. They showed, in particular, that the currents of interest here can be expressed as

$$\begin{aligned} \mathbf{J}_1 &= -\left[\frac{D_T}{T}\,\nabla T + D\,T\,\nabla(\frac{\mu}{T})\right] \\ \mathbf{J}_e &= -\left[\kappa\,\nabla T + D_T\,T\nabla(\frac{\mu}{T})\right] \end{aligned} \tag{1}$$

where κ is the coefficient of thermal conductivity (as in the Fourier law), D is the mutual diffusion coefficient (as in Fick's law) and D_T the coefficient of thermal diffusion (as in Soret's effect). The equations above refer to the case, considered in the following, of an isotropic system. In the more general case, e.g. liquid crystals, the thermal conductivity is in fact a tensor. Note that here and in the following we adopt the notation of Trimble and Deutch to identify the thermal transport coefficients and the relevant fields (see, for example, the discussion in the Appendix of Trimble and Deutch[25] for a review of possible alternative definitions). In the same paper[25], expressions for the transport coefficients in terms of time correlation functions were obtained.

The connection between the coefficients computed via time correlation functions at equilibrium and quantities directly accessible to experiments, however, is problematic for mixtures because it requires auxiliary calculations of thermodynamic quantities such as partial enthalpies and derivatives of the chemical potential[26,27]. The exception is the mutual diffusion coefficient D for which a straightforward Green-Kubo expression is established[25]. Moreover, useful relationships exist for the thermal transport coefficients and energy current

densities in the, non-equilibrium, stationary states[25]. When combined, as discussed below, these relationships make it possible to compute the thermal conductivity and diffusion coefficients more straightforwardly. In this work, we propose to take advantage of this observation to define a suitable computational approach. To see how, we recall that for a system subject to a temperature gradient the stationary state is such that

$$\begin{aligned} \mathbf{J}_1 &= 0 \\ \mathbf{J}_e &= -\left[\kappa - \frac{D_T^2}{DT}\right]\nabla T \equiv -\lambda_T \nabla T \end{aligned} \tag{2}$$

where the coefficient λ_T is defined implicitly in the last equation. The thermal and mutual diffusion coefficients are related, in the definition of the Soret coefficient of the mixture[6], by $S_T = D_T/D$. This coefficient, accessible also in experiments, provides a measure of the relative strength of thermally induced and concentration driven diffusion. In the following, we shall consider an equimolar mixture in which the thermal gradient is directed along the z axis. In this case, the Soret coefficient can be measured directly, in stationary conditions, as[4]

$$S_T = -4\left(\frac{\partial \chi_1}{\partial z}\right)\left(\frac{\partial T}{\partial z}\right)^{-1} \tag{3}$$

where χ_1 is the mole fraction of species 1.

Based on the observations above, all the thermal transport coefficients can be computed from atomistic simulations by combining equilibrium and non-equilibrium molecular dynamics simulations. Our approach can be summarized as follows. Equilibrium MD will be used to obtain the mutual diffusion coefficient D by computing the time correlation function of the mass current of species 1 in the system. Non-equilibrium MD will instead be used to simulate the binary mixture under the constant thermal gradient and access quantities in the steady state. D-NEMD will be employed to characterize the transient and to verify the establishment of the steady state by following the evolution of the density and temperature fields, and of the associated currents, from the appearance of the thermal gradient to sta-

tionarity. In the stationary condition, a direct measurement of the energy flux at a known value of the thermal gradient will provide us with an estimate of the thermal coefficient $\lambda_T = \left[\kappa - \frac{D_T^2}{D\,T}\right]$, while the ratio of the slope of the density (related to the mole fraction) and temperature fields will measure the Soret coefficient. From these calculations we can obtain

$$\begin{aligned} D_T &= D\,S_T \\ \kappa &= \lambda_T + \frac{D\,S_T^2}{T} \end{aligned} \tag{4}$$

Simulation methods and microscopic expressions of observables

As mentioned in the Introduction, the non-equilibrium molecular dynamics simulation will be performed using the D-NEMD approach[22]. This method implements numerically the Onsager principle on the regression of fluctuations[23,24] and has been applied to a variety of problems[28–35], including a preliminary investigation of the Ludwig-Soret effect[20]. In this approach, the binary mixture is described at a microscopic level as a system of N_α particles of each species ($\alpha = 1, 2$ is the species index) in the phase space $\Gamma \equiv \{\mathbf{r}_{i_1}, \mathbf{p}_{i_1}, \mathbf{r}_{i_2}, \mathbf{p}_{i_2},\ i_1 = 1, \ldots, N_1,\ i_2 = 1, \ldots, N_2\}$, where $\mathbf{r}_{i_\alpha}, \mathbf{p}_{i_\alpha}$ are the positions and momenta of particle i of species α. The time evolution of the system is governed, at equilibrium, by the (time-independent) Hamiltonian $H_0(\Gamma)$, and time evolution operator $S_0(t)$ such that $\Gamma_t = S_0(t)\Gamma$, where we have indicated with Γ_t the phase space point at time t, and for convenience of notation, we assume that the initial time of the evolution is $t_0 = 0$, using the notation $\Gamma_{t_0} = \Gamma$.

According to the prescriptions of statistical mechanics, a generic macroscopic field, indicated as $O(\mathbf{r}, t)$, can be obtained as the ensemble average of the corresponding microscopic observable over phase space. If we indicate this microscopic observable as $\hat{O}(\mathbf{r}, \Gamma) \equiv$

$\sum_{k=1}^{N} O_k(\Gamma)\delta(\mathbf{r}-\mathbf{r}_k)$, we then have

$$O(\mathbf{r},t) = \int d\Gamma \hat{O}(\mathbf{r},\Gamma) f(\Gamma,t) \tag{5}$$

where $f(\Gamma,t)$ is the, normalized, phase space probability density of a time dependent ensemble. The expression above can be re-expressed identically by first observing that the evolution of the probability density under a time dependent dynamics from time $t_0 = 0$ can be written, due to the Liouville equation, as $f(\Gamma,t) = S^{\dagger}(t) f(\Gamma,0)$, while for an observable the evolution operator is the adjoint, i.e. $\hat{O}(\mathbf{r},\Gamma_t) = S(t)\hat{O}(\mathbf{r},\Gamma)$. Here we indicate with $S(t)$ the evolution operator of the time-dependent dynamics. Using the definition of the scalar product in Hilbert space to transfer the evolution from the probability density to the microscopic observable, we have

$$\begin{aligned} O(\mathbf{r},t) &= \int d\Gamma \hat{O}(\mathbf{r},\Gamma)\left[S^{\dagger}(t) f(\Gamma,0)\right] \\ &= \int d\Gamma \left[S(t)\hat{O}(\mathbf{r},\Gamma)\right] f(\Gamma,0) \\ &= \int d\Gamma \hat{O}(\mathbf{r},\Gamma_t) f(\Gamma,0) \end{aligned} \tag{6}$$

The last equation, known as the Kubo-Onsager relationship, provides the formal basis for D-NEMD[36,37]. It states that the time evolution of a macroscopic field can be obtained as the average over the ensemble at the initial time of the time evolved microscopic observable. The time evolution of the microscopic observable can be obtained via MD for quite general dynamical systems. If the probability density $f(\Gamma,0)$ can be sampled by simulation (e.g. when it corresponds either to equilibrium or to stationary conditions) then, the relationship above generates the D-NEMD algorithm to calculate the fields.

This algorithm can be summarized in three steps (see also figure 1):

(1) sample a set of initial conditions from $f(\Gamma,0)$ (e.g. at equilibrium using Monte Carlo or molecular dynamics driven by H_0);

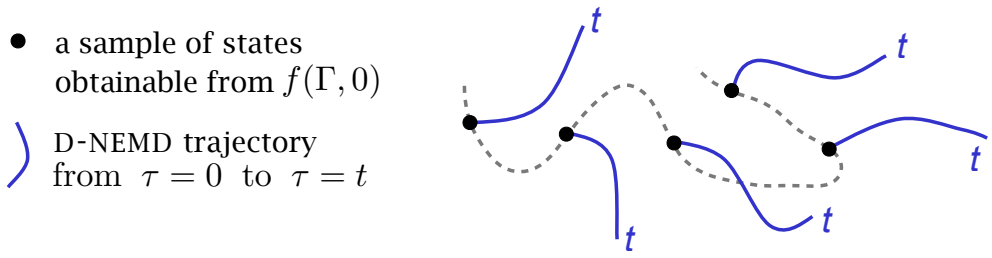

Figure 1: Scheme of the D-NEMD algorithm: A set of individual trajectories (segments), started from initial conditions sampled from $f(\Gamma, 0)$ is propagated for a time t based on the non-equilibrium dynamics to which the system is subjected. The time-dependent non-equilibrium average is then obtained as the mean of the values of the observable $\hat{O}(\mathbf{r}, \Gamma_t)$ computed along each segment.

(2) evolve these initial configurations under the non-equilibrium dynamics of the system and compute the microscopic observable along each trajectory;

(3) compute the macroscopic field as the average of the microscopic observable over the trajectories.

As mentioned in the previous subsection, we shall study the Ludwig-Soret effect in an equimolar Ar-Kr mixture, with constant thermal gradient directed along the z axis of the system. The macroscopic fields relevant for this phenomenon are the number density field of the species and the temperature field. The corresponding microscopic observables are defined as (in all equations below $\alpha = 1, 2$)

$$\hat{n}_\alpha(\mathbf{r}, t) = \sum_{i_\alpha=1}^{N_\alpha} \delta(\mathbf{r}_{i_\alpha}(t) - \mathbf{r}) \tag{7}$$

and

$$\hat{T}(\mathbf{r}, t) = \frac{1}{3k_B} \sum_\alpha \sum_{i_\alpha=1}^{N_\alpha} \frac{\tilde{\mathbf{p}}_{i_\alpha}^2(t)}{m_\alpha} \delta(\mathbf{r}_{i_\alpha}(t) - \mathbf{r}) \Bigg/ \left(V \sum_\alpha \langle \hat{n}_\alpha(\mathbf{r}, t) \rangle - 1 \right) \tag{8}$$

In the equation above, $\tilde{\mathbf{p}}_{i_\alpha}(t)$ is the momentum in the center of mass reference, i.e. $\tilde{\mathbf{p}}_{i_\alpha}(t) = \mathbf{p}_{i_\alpha}(t) - m_\alpha \mathbf{v}_{cm}$, where $\mathbf{v}_{cm}$ is the center of mass velocity, V the volume of the system, and k_B is the Boltzmann constant. In all calculations discussed in the following, $\mathbf{v}_{cm} = 0$ and so we drop the tilde on the momenta to simplify the notation. The brackets in eq. (8) indicate

an average with respect to the initial ensemble at $t_0 = 0$ while, consistent with eq. (6), the time evolution is that of the system subject to the thermal gradient. A detailed description of the equilibrium sampling and non-equilibrium dynamics are given in sections Simulation set-up and Results and Discussion. To the density and temperature fields are associated the mass current for each species

$$\hat{\mathbf{J}}_\alpha(\mathbf{r},t) = \sum_{i_\alpha=1}^{N_\alpha} \mathbf{p}_{i_\alpha}(t)\,\delta(\mathbf{r}_{i_\alpha}(t)-\mathbf{r})\,, \tag{9}$$

and the energy current[13,38]

$$\begin{aligned}\hat{\mathbf{J}}_e(\mathbf{r},t) &= \sum_{\alpha=1}^{2}\sum_{i_\alpha=1}^{N_\alpha} e_{i_\alpha}(t)\,\frac{\mathbf{p}_{i_\alpha}(t)}{m_\alpha}\,\delta(\mathbf{r}_{i_\alpha}(t)-\mathbf{r}) \\ &+ \frac{1}{2}\sum_{\alpha=1}^{2}\sum_{\beta=1}^{2}\sum_{i_\alpha=1}^{N_\alpha}\sum_{j_\beta=1}^{N'_\beta}\left[(\mathbf{r}_{i_\alpha}(t)-\mathbf{r}_{j_\beta}(t))\cdot\mathbf{F}_{i_\alpha j_\beta}(t)\right]\frac{\mathbf{p}_{i_\alpha}(t)}{m_\alpha}\,\delta(\mathbf{r}_{i_\alpha}(t)-\mathbf{r})\end{aligned} \tag{10}$$

where

$$e_{i_\alpha}(t) = \frac{\mathbf{p}^2_{i_\alpha}(t)}{2m_\alpha} + \frac{1}{2}\sum_{\beta=1}^{2}\sum_{j_\beta=1}^{N'_\beta}\phi(\mathbf{r}_{i_\alpha}(t),\mathbf{r}_{j_\beta}(t)) \tag{11}$$

where $\phi(\mathbf{r}_{i_\alpha},\mathbf{r}_{j_\beta})$ is the (pair) potential between particle i of species α and particle j of species β, and the prime indicates that self interactions must not be considered. $\mathbf{F}_{i_\alpha j_\beta} = -\nabla_{i_\alpha}\phi(\mathbf{r}_{i_\alpha},\mathbf{r}_{j_\beta})$ is the force on particle i of species α due to particle j of species β.

As mentioned above, see eq. (3), given the symmetry used in our simulation, the ratio of the slopes of $n_1(\mathbf{r},t)$ (which can be related to the mole fraction) and $T(\mathbf{r},t)$ in the steady state will allow us to measure the Soret coefficient, while the ratio of the constant energy flux over the imposed constant thermal gradient, see second line of eq. (2), will provide an estimate of λ_T. Finally, the mutual diffusion coefficient (to be computed from equilibrium molecular dynamics simulations) is defined as[25]

$$D = \lim_{t\to\infty}\frac{1}{3k_BTV}\int_0^t ds\langle\hat{\mathbf{J}}_1(s)\cdot\hat{\mathbf{J}}_1(0)\rangle \tag{12}$$

The estimate of the thermal transport coefficients outlined above requires a precise measurement of the currents. The averages of these quantities, however, present a significant level of noise that hides the behavior of the system both in the transient and in the steady state, and prevents converging the D-NEMD calculation with reasonable computational effort[20] . The problem affects all the currents, but, as shown in the following, it is particularly critical for the mass current $\hat{\mathbf{J}}_1$ of species 1. It is, however, possible to mitigate this difficulty by observing that the typical time scales over which the currents show significant changes are considerably longer than those corresponding to the natural microscopic evolution of the system. One can then take advantage of this fact to smooth the, slow varying, noisy signal by averaging it over short time segments on each D-NEMD trajectory. The final signal is then constructed as the mean of the short time averages on the ensemble of trajectories. By indicating with $X(t)$ the noisy signal in the time interval $[t_0, t_f]$, the smoothed estimator on each trajectory is given by

$$\hat{\mu}(\tau) = \frac{1}{\tau_w} \int_{-\tau_w/2}^{\tau_w/2} X(\tau + s) ds \tag{13}$$

where τ_w is the time width of the averaging window (nb. in the time intervals $\tau \in [t_0, t_0 + \tau_w]$ and $\tau \in [t_f - \tau_w, t_f]$, the limits of integration and the normalization are adjusted accordingly to the available window, centered around τ). The stability of this smoothing procedure can be verified by varying the width of time window over which the average is taken along each trajectory. Note that this approach still preserves the full average over the whole set of non-equilibrium initial conditions and is therefore very different from attempts to obtain non-equilibrium properties from long time averaging along a single trajectory.

Simulation set-up

We study an equimolar Kr-Ar mixture in which the atomic interactions are described by Lennard-Jones potentials. Lennard-Jones units $\sigma = 1,\ \epsilon = 1,\ m = 1$ referred to Argon are

adopted throughout, with potential parameters for Krypton equal to $\sigma_1 = 1.07\,\sigma$, $\epsilon_1 = 1.39\,\epsilon$ and $m_1 = 2.1\,m$. Pair interactions between particles of different species follow the Lorentz-Berthelot convention, $\sigma_{12} = \sigma_{21} = (\sigma_1 + \sigma_2)/2$ and $\epsilon_{12} = \epsilon_{21} = \sqrt{\epsilon_1 \epsilon_2}$.

All simulations are carried out at the reference (total) number density $n^* = 0.7256\,\sigma^{-3}$ and reference (mean) temperature $T^* = 1.0\,\epsilon/k_B$. The simulation boxes (see also figure 2), are rectangular prisms whose linear dimensions are taken as integer multiple of the potential cut-off distance r_c. This choice makes it possible to optimize, using the cell index method[39], adopted in the simulations, the calculation of pair interactions with orthorombic periodic boundary conditions enforced in all directions. The macroscopic fields are estimated by discretizing the space only along the z axis, i.e the direction of the temperature gradient, since the fields remain uniform in the orthogonal directions, as checked in our preliminary study[20] (see also Results section). The simulation box was divided into parallel slabs of width $\Delta z = \sigma_1$, each identified by its middle point along the $z-$axis: $z_M = (M - \frac{1}{2})\sigma_1$ with $M = 1, 2, \ldots, M_{max}$. A cut-off distance $r_c = 3\,\sigma_1$, i.e. equal to three times the discretization spacing Δz, was used for all interactions in all simulations. This value, somewhat larger than the 2.5σ cut-off usually adopted with Lennard-Jones interactions, suits better the space discretization and helps reducing the truncation noise in the calculation of the energy current, eq.(10), without a significant increase of the cost of the calculation.

The equilibrium simulations are performed on a box of dimensions $(6r_c \times 6r_c \times 6r_c)$ containing 5184 particles (i.e. $N_1^{(eq)} = 2592$). The non-equilibrium runs are performed on a larger system of 11760 particles (i.e. $N_1^{(ne)} = 5880$) and box dimensions $(7r_c \times 7r_c \times 10r_c)$, the largest dimension referring to the $z-$axis. In these simulations $M_{max} = 30$ slabs were employed, each containing, on average, 392 atoms. To drive the systems to the desired temperature and to establish the thermal gradient, we employ a scheme in which the velocity rescaling is applied to the particles within selected regions of the simulation box to match a prescribed average target temperature. The position of the thermostatted regions can be arbitrarily chosen and particles are free to move in and out of them. In the set-up

adopted in this work, these regions correspond to three consecutive slabs located one at the left ($M = 1, 2, 3$) and the other at the right boundary ($M = 28, 29, 30$) along the $z-$direction of the simulation box. With this set-up the thermostatted regions share a common interface due to the periodic boundary conditions and there is a unique region of interest in the central part of the box ($M = 4, ..., 27$) over which a single uniform thermal gradient is established. Only particles in this region contribute to the calculated signals. Note that, since the thermostatting regions have a width at least equal to r_c, particles in the physically relevant central part of the box can interact at most with particles in one of the two thermostatted regions regardless of periodic boundary conditions. This simulation set-up differs from the one adopted to compute the Soret coefficient, for example, in the so-called reverse perturbation nonequilibrium molecular dynamics (RPNMD) approach[40]. In this alternative set-up, imposed mainly by the practical implementation of the specific scheme enforced to establish stationary non-equilibrium currents[4], the cold and hot thermostats are placed at one of the edges and at the center of the simulation box. Due to periodic boundaries, this results in two separate regions of interest in the box where thermal gradients of equal magnitude but opposite sign are established. In preliminary calculations, we have experimented with these two different set-ups and verified that results for the stationary gradients and transport properties, in particular for the Soret coefficient, are the same. The simulation scheme adopted in the following was chosen because it maximises the number of independent samples obtained, at equal computational effort, for the transient behavior by avoiding dynamical correlations in the evolution of the fields which are present when using the RPNMD set-up. The thermostatted regions, identified with the letters C (*cold*) and H (*hot*) are kept at the temperature T_C and at the temperature T_H, respectively. When thermostatting the system to sample initial conditions from the 'equilibrium' distribution the two values are equal to the assigned target temperature $T_H = T_C = T^*$, while to establish a ΔT thermal gradient around the mean value T^*, the two temperatures values $T_C = T^* - \Delta T/2$ and $T_H = T^* + \Delta T/2$ are imposed. The dynamics of the particles

is integrated using the standard velocity-Verlet algorithm, with an additional step, which implements the local temperature control, for the dynamics of the particles inside the two thermostatted regions. After their dynamics is propagated with the usual velocity-Verlet scheme, the (local) kinetic energy and (local) momentum are computed within each slab. Then particle velocities are rescaled in such a way that, within each slab, the (local) kinetic energy matches the target temperature while the (local) momentum does not change. More in detail, velocity rescaling is performed as follows. At each timestep, the center of mass velocity of the particles in the slab is computed as

$$\mathbf{v}_M(t) = \sum_{\alpha} \sum_{j_\alpha \in M} \mathbf{p}_{j_\alpha}(t) / \sum_{\alpha} \sum_{j_\alpha \in M} m_\alpha \tag{14}$$

where the index M can refer either to a slab in the cold region, i.e. $M = 1, 2 \text{ or } 3$ or to a slab in the hot region, i.e $M = 28, 29 \text{ or } 30$. The (local) instantaneous kinetic energy, excluding the center of mass motion, in the M-th slab is then calculated as

$$\mathcal{K}_M(t) = \sum_{\alpha} \sum_{j_\alpha \in M} \frac{(\mathbf{p}_{j_\alpha}(t) - m_\alpha \mathbf{v}_M(t))^2}{2m_\alpha} \tag{15}$$

and used to obtain the scaling factor

$$\gamma_M = \sqrt{\frac{2\mathcal{K}_M(t)}{3(N_M(t) - 1)k_B T_M}} \tag{16}$$

where $N_M(t) = \sum\limits_{\alpha} \sum_{i_\alpha \in M} 1$ is the total number of particles in the M-th slab at the time t and T_M the target temperature. The particles are finally assigned new momenta defined as

$$\bar{\mathbf{p}}_{j_\alpha}(t) = \gamma_M(\mathbf{p}_{j_\alpha}(t) - m_\alpha \mathbf{v}_M(t)) + m_\alpha \mathbf{v}_M(t) \tag{17}$$

As mentioned above, this procedure ensures that, layer by layer, the thermostat does not influence the momentum density and, as a consequence, the total momentum of the whole

system in the simulation box is a constant of motion of the dynamics. Numerical conservation, within the round-off noise, of the total momentum, set to zero at the initial time, was monitored and verified in all simulations. The scheme described above is a refinement of the one proposed in our preliminary calculations[20] and of similar algorithms developed for the simulation of convective cells[31] and steady state calculations of thermal transport coefficients[4,41]. Note that, as the number of particles in the inner, non-thermostatted region can vary, the ensemble generated in this way is not strictly canonical at equilibrium, however this was verified not to have detectable consequences in our simulations.

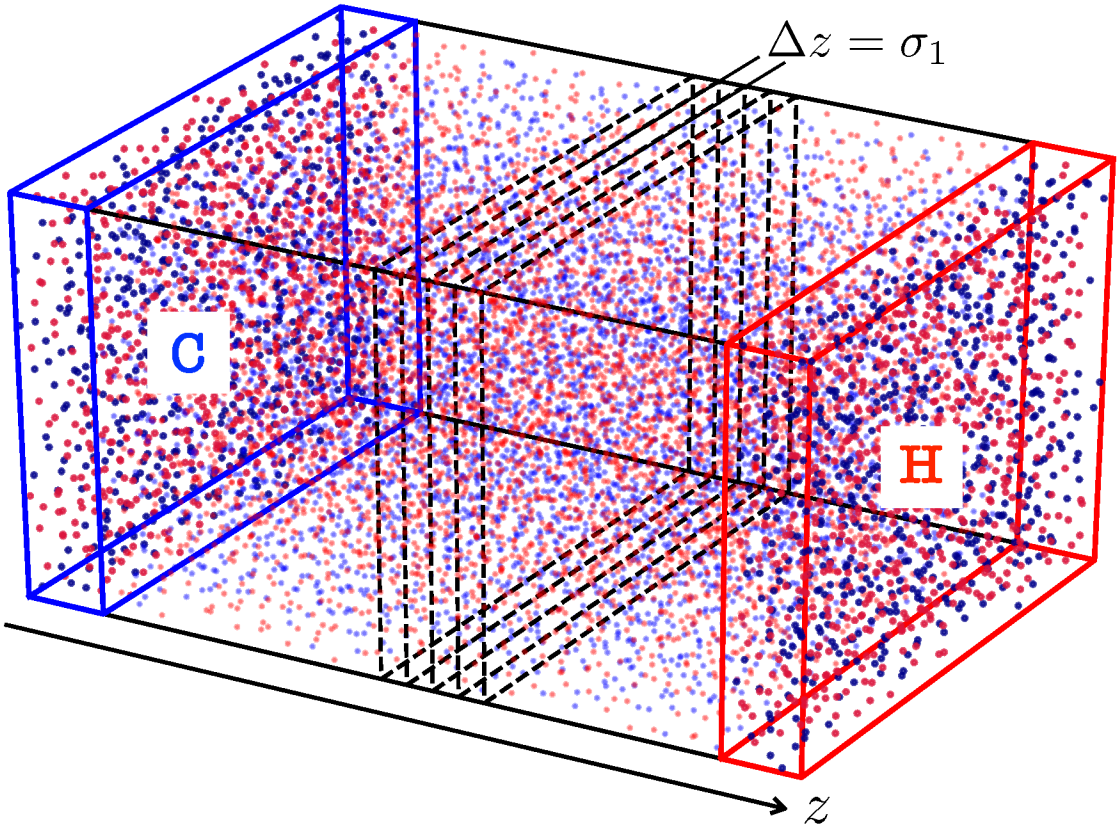

Figure 2: Snapshot of the simulation box. Kr atoms are colored in red, Ar atoms in blue. Particles in the region H and in the region C, are identified by using larger markers and more saturated colors compared to those in the bulk region. Periodic boundary conditions are applied in all directions and the discretization of space along the z direction is illustrated with dashed lines in part of the central region.

Results and discussion

The results presented in the following were obtained via the D-NEMD scheme, implemented by considering an ensemble of initial conditions sampled from an equilibrium MD trajectory in which the system has a homogeneous temperature equal to $T^* = 1\epsilon/k_B$. A non-equilibrium trajectory is started from each initial condition by imposing, at $t_0 = 0$, the thermal gradient along the z direction. The gradient is generated by changing the temperatures at the boundaries of the simulation box as described in the previous section, resulting in a temperature difference between the cold and hot boundary equal to $\Delta T = 0.1\epsilon/k_B$. The non-equilibrium trajectories are propagated using a timestep $\delta t = 0.005$ in reduced Lennard-Jones units.

Results for the fields and fluxes are presented as a function of the z coordinate alone, (i.e. in the direction of the thermal gradient) since the components along the x and y directions of the currents vanish on average. Correspondingly, the density and temperature fields are constant along the x and y directions. We denote the z component of the mass current of Kr as $J_1(z,t)$ (no boldface), with analogous notation for the other quantities , (dropping the $z-$component suffix to simplify the notation). For each trajectory, the estimators for the fields in the M-th slab are obtained by discretizing the sum over the Dirac *delta*-functions. In correspondence of the field position $\mathbf{r} \longrightarrow z_M$, one has $\sum_{i_\alpha} \delta(\mathbf{r}_{i_\alpha} - \mathbf{r}) \longrightarrow \frac{1}{V_M} \sum_{i_\alpha \in M}$ where the sum runs over the particles of species α in slab M. For example, the estimator for the density $\tilde{n}_\alpha(z_M, t)$ is defined as

$$\tilde{n}_\alpha(z_M, t) = \frac{N_M^\alpha(t)}{V_M} \tag{18}$$

where $N_M^\alpha(t) = \sum_{i_\alpha \in m} 1$ is the number of particles of species α in the $M-$th slab at time t and V_M is the volume of the $M-$th slab (equal for all of them). The estimator for the momentum density field $\mathbf{G}(z_M, t)$ is defined as

$$\tilde{\mathbf{G}}(z_M, t) = \left(\sum_\alpha \sum_{j_\alpha \in M} m_\alpha \right) \mathbf{v}_M(t) \tag{19}$$

and, for the equimolar mixture under consideration, the estimators of the partial temperature fields $\tilde{T}_\alpha(z_M, t)$ in each slab, are given by

$$\tilde{T}_\alpha(z_M, t) = \frac{2\tilde{K}_\alpha(z_M, t)}{3k_B} \Big/ \langle N_M^\alpha(t) - m_\alpha / \sum_\beta m_\beta) \rangle \tag{20}$$

where

$$\tilde{K}_\alpha(z_M, t) = \sum_{j_\alpha \in M} \frac{\left[\mathbf{p}_{j_\alpha}(t) - m_\alpha \mathbf{v}_M(t)\right]^2}{2m_\alpha} \tag{21}$$

is the kinetic energy of the particles of species α in the $M-$th slab calculated excluding the corresponding fraction of the degrees of freedom for the center of mass motion $\mathbf{v}_M$. The correction to the number of degrees of freedom in eq.(20) is distributed proportionally to the mass of each species. The discretized estimators for the current fields $\tilde{\mathbf{J}}_e(z_M, t)$ in eq. (9) and $\tilde{\mathbf{J}}_1(z_M, t)$ eq. (10) are defined in analogy with those for the number and momentum densities and for the temperature fields.

The macroscopic fields are computed by averaging the microscopic estimators over an ensemble of 2000 D-NEMD non-equilibrium trajectories. When necessary, in particular for the currents, the smoothing scheme described in the previous section was implemented to regularize the final average. Details on the width of the averaging window are given in the text and in the appropriate figure captions.

The transient regime

Figures 3 and 4 show the short, $t \in [0, 100]$, and long, $t \in [100, 2000]$, time behavior of the temperature field $T(z, t)$ (left panel) and of the number density $n(z, t) = (n_1(z, t) + n_2(z, t))$ (right panel), as functions of the z coordinate. Figure 3 indicates that switching on the thermal gradient rapidly induces an intermediate state in which these fields (and thus the total temperature and density fields) change from their equilibrium values, constant along z in the non thermostatted part of the box, (red curves in the figure) to a linear profile which is reached by $t = 40$ (blue curve) and remains essentially constant thereafter (purple, $t = 50$,

and magenta, $t = 100$, curves). For both fields, the action of the thermostats induces a gradual change that propagates from the sides to the center of the box. The final temperature

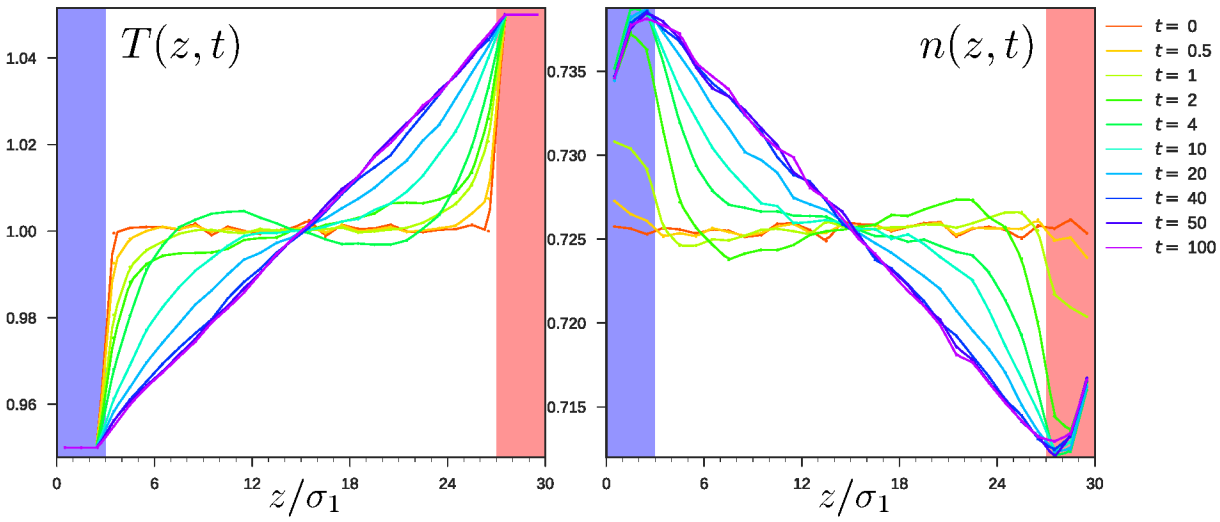

Figure 3: Dynamical behavior of the temperature (left panel) and density (right panel) profiles at short times as a function of the, discretized, z coordinate. The color code indicates the different times at which the fields are shown, with values in the legend on the right valid for both panels.

profile is perfectly consistent with the imposed gradient from the cold thermostat (blue area in the figure) to the hot thermostat (red area). The linear profile of the density has opposite slope compared to the temperature, showing an average accumulation of particles towards the cold region. The main characteristics of these fields are established on this fast time scale and maintained up to and in the stationary state. Indeed, figure 4 demonstrates that for longer times, $t > 100$, the average temperature and the total density do not change, with the latter showing only minor fluctuations. The time evolution of the temperatures of each species (not shown) is essentially superimposed to that of the average temperature. The time evolution of the number density profiles of the individual species, on the other hand, shows a more intricate behavior that develops over a much longer time scale. Let us begin by considering the evolution of the Kr and Ar densities at short times, shown in the left and right panel of figure 5, respectively. Immediately after the thermal gradient is switched on, the densities manifest relevant variations near the thermostats. For both species there

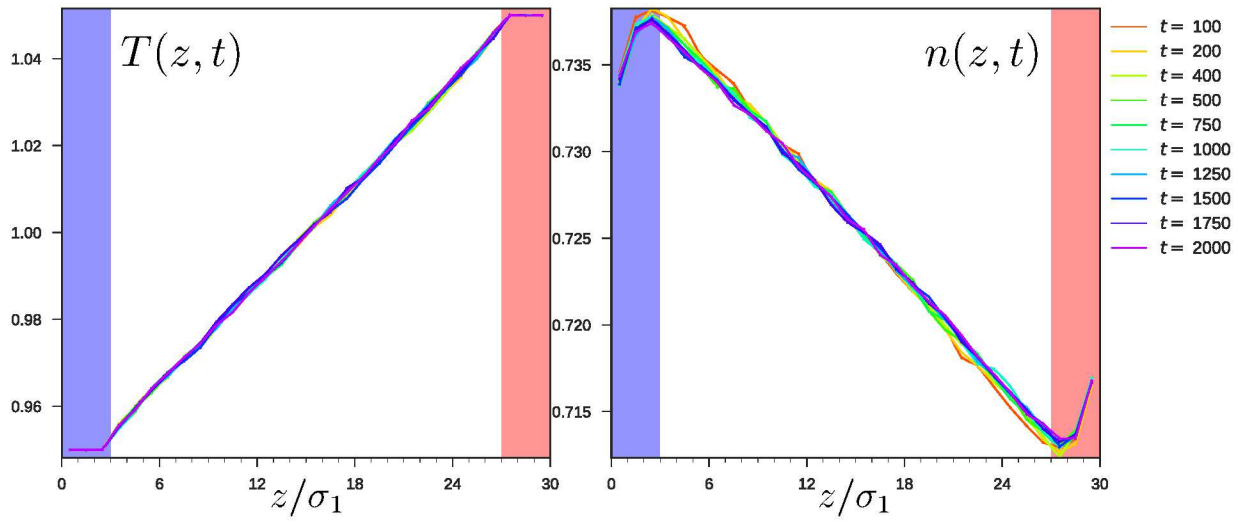

Figure 4: Dynamical behavior of the density and temperature profiles as a function of the discretized z coordinate at longer times. As in the previous figure, the panel on the left is temperature, the panel on the right density. Color codes for curves refer to different times as indicated in the legend on the right.

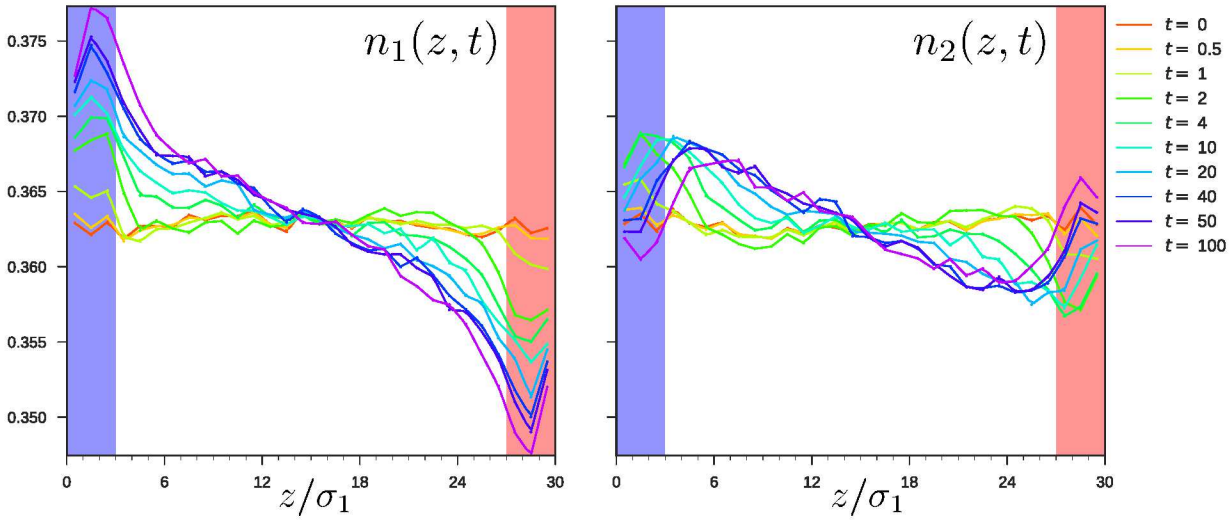

Figure 5: Dynamical behavior of the density profile for each species at short times. (time increases from red, initial time, to magenta, $t = 100$. Color codes are the same as for figure 3): Left panel is the Kr density and right panel is the Ar density.

is an initial, $t \in [1, 40]$, increase of the density in the cold region, and a decrease near the higher temperature thermostat. As time progresses, this leads to an essentially monotonic increase of the slope of the density profile for Kr with progressive separation of the values on the left and right of the system and smoothing of the profile. This trend continues at longer times, see left panel of figure 6, and the profile becomes linear at $t \approx 1500$ stabilizing around its stationary state. The evolution of the Ar density is more complex. The initial,

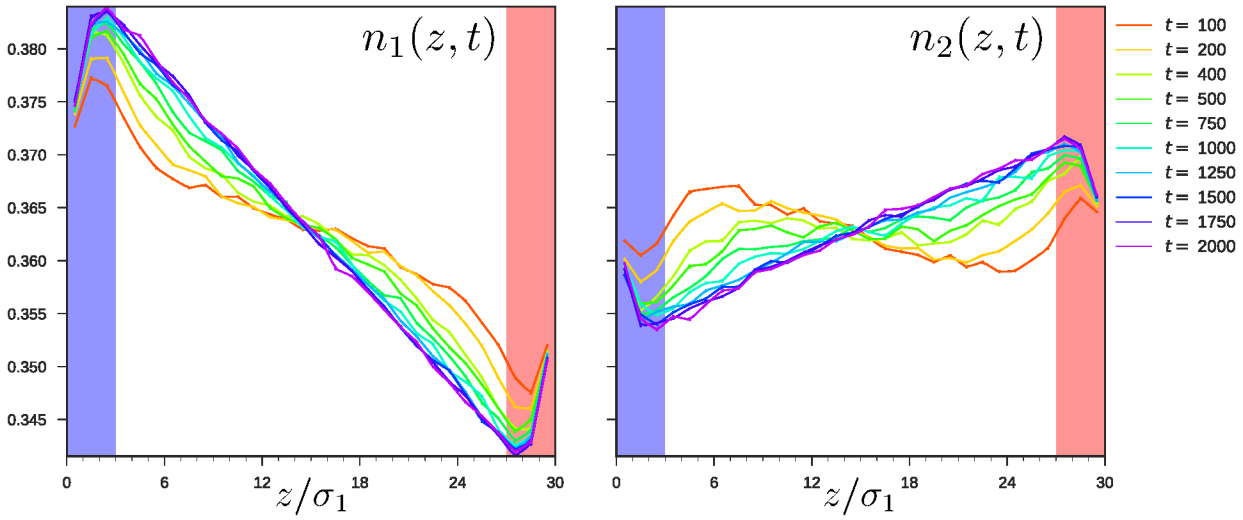

Figure 6: Dynamical behavior of the density profiles for each species at longer times, the left panel reports the Kr density field, the right panel shows the Ar density field. (Color codes are the same as for figure 4).

$t \leq 40$, increase at the cold boundary is followed by a depletion near the thermostat which progressively shifts the maximum of the profile. At $t = 100$ (magenta curve in figure 5 and red curve in figure 6) an oscillation of the density, with inflection at the center of the box and a trend showing and overall left to right slope, is clearly visible. As time progresses, right panel of figure 6, the Ar density evolves further, first by flattening the profile and eventually inverting the slope and becoming more and more linear for $t > 750$. The inversion of the trends of the density of the two species is therefore a slow process, appearing around $t \gtrsim 100$, i.e. after the stabilization of the temperature and average density profiles, and becoming gradually more noticeable as the Soret effect builds up.

The different relaxation times for the total and single particle fields originate from the behavior of the currents, as verified by our simulations. To begin with, the onset of stationarity for the temperature and average density fields on a short time scale is confirmed by the behavior of the associated currents. In figure 7, we show the time evolution of the $z-$ component of the total momentum of the non-thermostatted particles, $G(t) = \left[\int_{V'} d\mathbf{r}\, \mathbf{G}(\mathbf{r},t)\right]_z$, i.e. the mass current, see eq. (19), integrated over the volume V' of the non-thermostatted part of the simulation box i.e. summing the discretized z-components of the estimator, see eq. (19), over the slabs with indices $M = 4, 5, \ldots, 27$. This value can be different from zero, and it is at any time equal to minus the same quantity calculated for the thermostatted parts of the simulation box, as the system total momentum is set to zero initially and remains so within machine precision. In this and in the other figures for the currents we report both the raw data, i.e. the simple average over the non equilibrium trajectories from the simulations, and the results obtained after time averaging over a window of width τ_w. In figures 7 and 8 the raw data is shown as black dots while the smoothed results are shown as red curves. The contribution from the z-component of the divergence of $\mathbf{G}(\mathbf{r},t)$ drives the time evolution of the total density. As expected, the integral of the momentum density $G(t)$ goes, quickly, to its stationary value, equal to zero. This value is in fact reached at about $t = 40$ in correspondence with the onset of stationarity for the total density. The relaxation shows clear oscillations on a time scale of about 7 Lennard-Jones time units, which is close to the time $\Delta\tau = 6.25$ that a longitudinal sound wave would need to cross the MD periodic cell along the z direction ($10r_c$ distance) with the sound velocity $c = 808$ m/s reported in ref.[42] for a equimolar mixture at $T = 0.975$. These oscillations probably originate from competing effects due to the time and space evolution of temperature and density fields: as the temperature wave propagates in the system, the resulting density wave creates a compression in the fluid in its direction of propagation. Particles then recoil due to the average effect of this compression front, before being pushed again by the temperature gradient. This is reflected in the momentum density, with the recoil effect probably amplified by the large temperature

gradients. Indeed The typical values of $G(t)$ show an oscillation range spanning about 100 Lennard-Jones units at short time. This results in a good signal to noise ratio with the ensemble size adopted in our calculations, and enables to obtain a well converged signal by 'brute force', i.e. by simple averaging over non equilibrium trajectories. In this case, then, the (mild) time averaging performed over a time window $\tau_w = 1$, shown in red in the figure, results only in a minor smoothing effect on the curve.

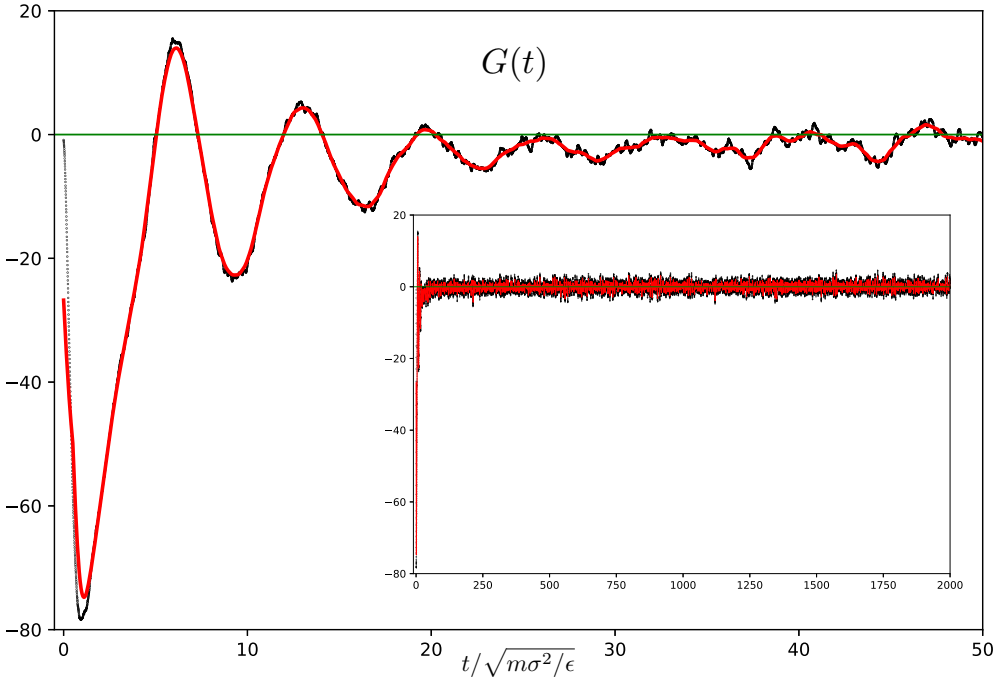

Figure 7: Momentum density, short time behavior: black dots represent the raw data while the red line is obtained by time averaging over a window of width $\tau_w = 1$ in Lennard-Jones time units (σ and ϵ in the axis label refer to Ar parameters). Beyond $t = 50$ the signal shows only statistical noise around zero, the stationary value, as shown in the inset.

Similar to the integral of the momentum density, $J_e(t)$, the energy current integrated over V' and reported in figure 8, shows a rapid decay for $t \in [0, 50]$, corresponding to the propagation of the thermal wave starting from the boundaries, penetrating and progressively reducing the plateau in the bulk as shown in the left panel of figure 3. For $t > 100$, the energy current becomes constant, consistent with eq. (2). Although this qualitative behavior is visible in the raw data (black points), the noise (average fluctuation) to signal ratio is equal to about 60%. In this case, the additional time averaging over a slightly larger time window,

$\tau_w = 4$, has a more pronounced effect in reducing the high frequency noise, as shown by the red curve in figure 8, enabling a more precise estimate of the thermal diffusion coefficient.

The time needed to reach the overall steady state of the system is, however, much longer than the one indicated by the energy current and this is reflected, as mentioned above, in the long time scale of the relaxation of the densities of the individual species. This can

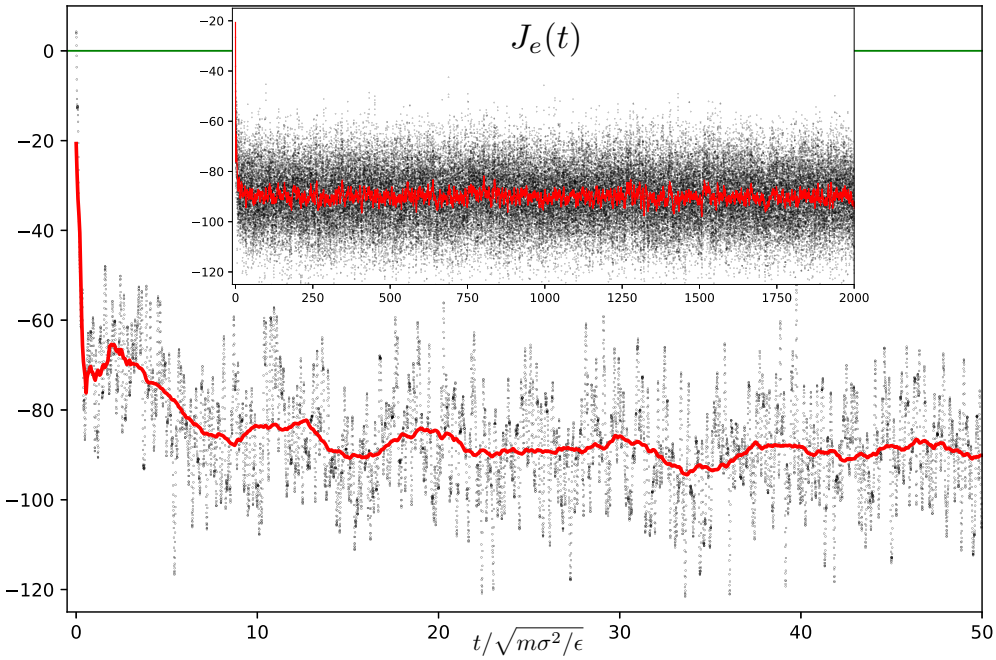

Figure 8: Short and long (inset) time behavior of the energy current $J_e(t)$. In the plots, the black dots represents the raw data and the red line is obtained by time averaging over a window of width $\tau_w = 4$ time units, given in Lennard-Jones units.

be appreciated also by considering the time evolution of the integrated mass current for Kr, shown in figure 9. Let us focus first on the bottom panel of the figure, showing the smoothed result. The plot indicates that there is an initial, relatively, fast increase in the current that at about $t \approx 100$ is followed by a slower relaxation towards the, stationary, zero value. Consistent with the evolution of the Kr density profile, the current becomes essentially null for $t > 1000$, showing fluctuations around zero for longer times as the profiles of both species stabilize around their final linear shape. The need for the time averaging procedure is clearly demonstrated by the top panel of figure 9 where we show as black dots the raw signal obtained by simple averaging over 2000 D-NEMD trajectories. The fluctuations of

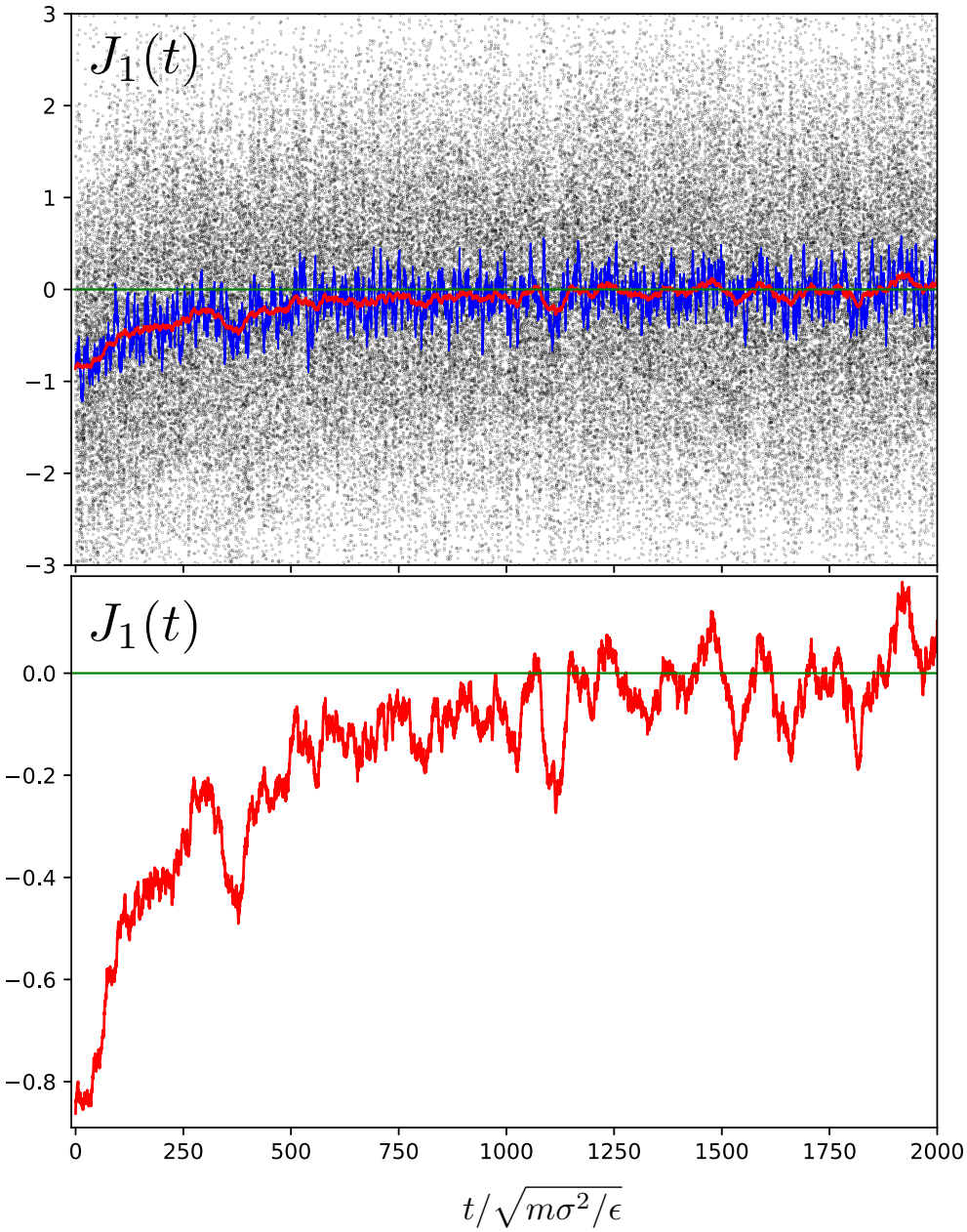

Figure 9: Kr mass current. In the top panel, black points show the raw data, while the blue and red curves present the smoothed results, with values of the time window width over which the average is taken equal to $\tau_w = 5$ (blue) and $\tau_w = 50$ (red) Lennard-Jones time units. The bottom panel reports the smoothed red curve for clarity of discussion.

the mass current are very large compared to the signal (these fluctuations are of the same order of those found for the integrated momentum density $G(t)$, which is, however, about two orders of magnitude larger) and essentially mask any trends. The blue and red curves superimposed to the raw data are the result of time averaging with two different window widths, a mild averaging $\tau_w = 5$ for the blue and a more aggressive one, $\tau_w = 50$ for the red curve, as reported in the caption. For both values of the smoothing parameter, the time averaging succeeds in discriminating the short and long time behavior of the field, making it possible, in particular, to identify the changes in the current from its initial negative values to zero and thus to verify that the system has reached its steady state. Note that, although a larger time window produces, as expected, a smoother signal (red vs blue curves) as more high frequency oscillations are averaged out, the red and blue curves are both stable and their overall characteristics show a converging behavior. The fact that the steady state is indeed attained on a time scale comparable to that of our simulations is confirmed by the time evolution of $J_1(z,t)$.

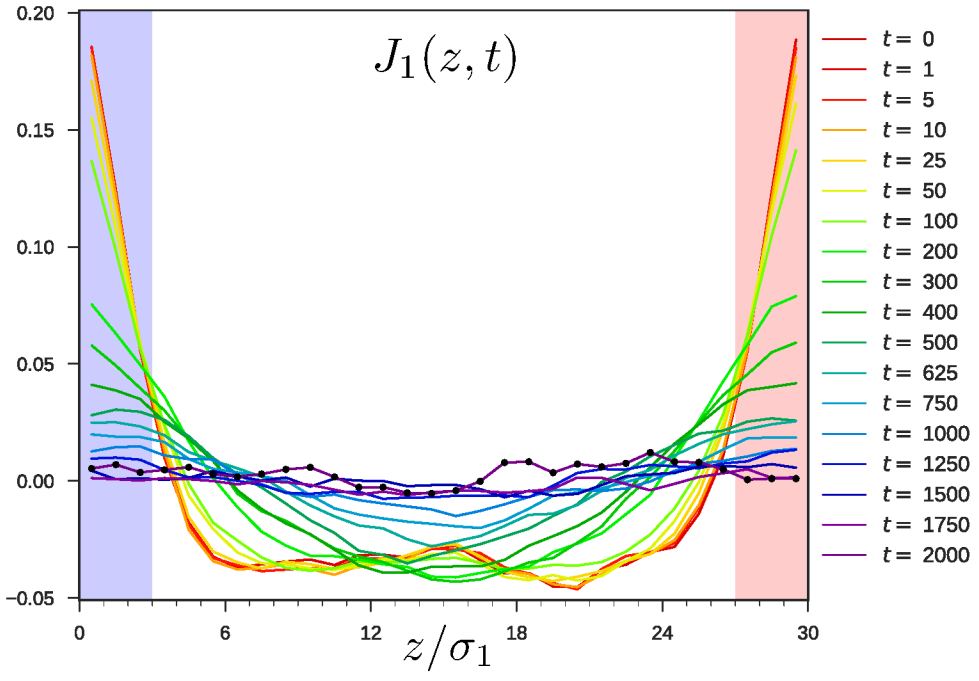

Figure 10: Dynamical behavior of the Kr mass flux, J_1, as a function of z and for different times (see color code on the right of the figure).

In figure 10, we show the history of the Kr mass current profile along z at different times obtained by applying an even more aggressive time averaging, with a width $\tau_w = 100$. The final time curve, identified by black dots in the plot, shows that the current is essentially converged, even though some fluctuations are still visible, to the expected zero value for all z.

Estimate of the transport coefficients

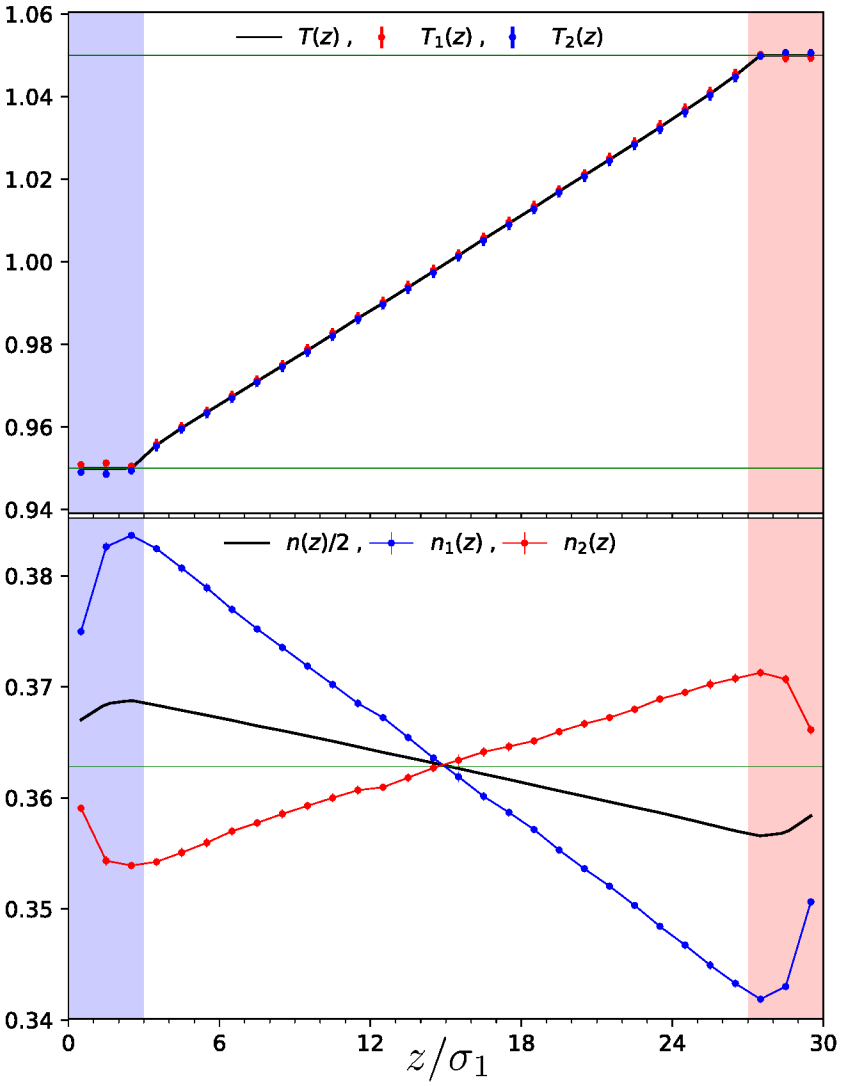

Figure 11: Temperature (upper panel) and density (bottom panel) fields in the stationary state. The green lines in the top panel show the temperature values set for the hot and cold thermostats. In the bottom panel, the green line indicates the half value of the fluid density ($n = 0.7256$).

Let us begin by summarizing, for convenience, the situation for the temperature and number density fields in the steady state. The results for these fields are presented in figure 11. In the top panel, we show in black, red and blue the temperature estimated from the *total*, Kr, and Ar kinetic energies, respectively, as a function of z (see eq. (8)). The dots correspond to averages over the kinetic energy of particles in each slab, with position indicated in units of $\Delta z \equiv \sigma_1$ in the abscissa. The bottom panel shows the stationary density profiles with the same color convention. From these curves, the slopes of the temperature and of the number density gradients were estimated. We obtained: $\frac{\partial T}{\partial z} = 0.003603 \pm 0.000016$ and $\frac{\partial n}{\partial z} = -0.000918 \pm 0.000008$, $\frac{\partial n_1}{\partial z} = -0.001575 \pm 0.000010$ and $\frac{\partial n_2}{\partial z} = 0.000657 \pm 0.000012$. Converting the number density in mole fraction, and using eq.(3) we get: $S_T = 2.41 \pm 0.02 = (20. \pm 0.2)\, 10^{-3}\mathrm{K}^{-1}$. This result is consistent with data for similar systems[4,20], though a direct comparison is delicate given the sensitivity of the Soret coefficient to small variations in the imposed temperature and density. For comparison, the average value of the Soret coefficient given by the model fitted with eq. (3) of Longree et al[5] is $< S_T >= 31 \times 10^{-3}\mathrm{K}^{-1}$ for an equimolar Ar-Kr mixture.

The value of the thermal conductivity can also be estimated from the steady state results, when $\bar{\mathbf{J}}_1 = 0$ and $\bar{\mathbf{G}} = 0$. Figure 8 shows that the energy current reaches a stationary, non vanishing, state with an asymptotic value $\bar{J}_e = -90.2$ from which we calculate, eq. 2, the "thermal conductivity"[25] $\lambda_T = \frac{\bar{J}_e}{V \nabla T} = 1.93 \pm 0.01$, both values in Lennard-Jones units. This value cannot be compared with similarly named quantities obtained via direct Green-Kubo formulas[9], or by response theory results obtained in non-equilibrium molecular dynamics by mechanical perturbations[10,11] since for a mixture the energy current cannot be identified with the heat flux nor immediately the mechanical perturbation with the thermal gradient.

The final input needed to compute the direct and cross Onsager coefficients is the mutual diffusion coefficient, D. As mentioned in the Methods, this quantity can be calculated from the equilibrium simulation of the system[25], since it is proportional to the time integral of the equilibrium autocorrelation function of the mass current of species 1. To compute

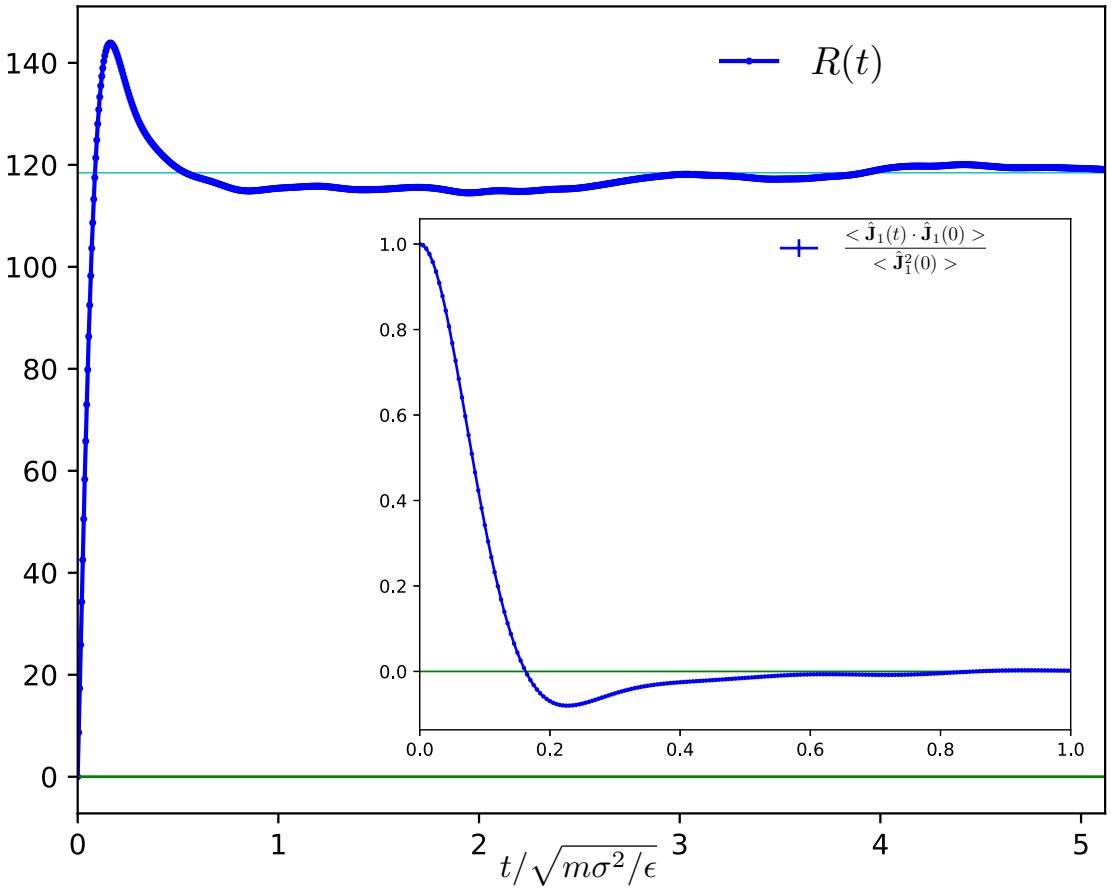

Figure 12: Autocorrelation (normalized) of $\hat{\mathbf{J}}_1$ and its running integral $R(t) = \frac{1}{3}\int_0^t \langle \hat{\mathbf{J}}_1(s) \cdot \hat{\mathbf{J}}_1(0)\rangle ds$ from equilibrium calculation.

it and the associated error, we propagated 16 independent NVE trajectories, each of 250 thousand steps (same timestep as in the non-equilibrium simulations). Initial conditions for these trajectories were sampled from an equilibrated NVT simulation, to ensure that the temperature was set to $T^* = 1\epsilon/k_B$. Figure 12 shows the mass current autocorrelation function, inset, and its integral, main figure. Both the shape and the decay times of the time correlation function are in good agreement with previous calculations[13]. Estimating the infinite time limit of the integral from the value of the plateau in the main figure, we get $D = \lim_{t\to\infty} \frac{R(t)}{k_B T V} = 0.0166 \pm 0.0001$ in Lennard-Jones units.

The value of the mutual diffusion coefficient can now be combined with our non-equilibrium measure of the Soret coefficient to obtain the thermal diffusion coefficient $D_T = DS_T = 0.0400 \pm 0.0006$ in Lennard-Jones units. Finally, from $\kappa = \lambda_T + DS_T^2/T$, eq. 2, we estimate the coefficient of thermal conductivity[25] $\kappa = 2.03$ in Lennard-Jones units. Comparison with experimental values in the literature is delicate, given the strong dependence on the thermodynamic point and only for the sake of completeness we report here the value $\chi = 4.43$ for the thermal conductivity measured by Mikhailenko et al. in similar conditions for temperatures but not for densities[43]. Results are summarized in Table 1.

Table 1: Summary of results for this calculation transport coefficients. All values are in Lennard-Jones units.

n^*	T^*	ΔT	$10^2 D$	S_T	λ_T	$10^2 D_T$	κ
0.7256	1.0	0.1	1.66 ± 0.01	2.41± 0.02	1.93 ± 0.01	4.00 ± 0.06	2.03 ± 0.02

Conclusions

In this paper, we have combined equilibrium and non-equilibrium simulations to obtain the full set of phenomenological coefficients appearing in the Onsager description of thermal transport. The transient behavior of the system was investigated in detail, to the best of our knowledge for the first time, using the D-NEMD approach to non-equilibrium simulations.

It presents a picture with a clear time scale separation between a fast regime, $t \approx 50$ in which the mixture behaves like a single component fluid, reaching a steady state for the temperature and overall density profiles, and a slow regime in which the behavior of the species differentiates and the Ludwig-Soret effect builds up. The time evolution of the Ar (lighter species in our mixture), in particular, is non trivial, following the profile of the average density for short times, building a definite oscillation and then inverting its overall slope to relax to its linear stationary profile on the longer time scale. In the stationary regime the momentum current of the fluid vanishes while a steady heat flux from the hot to the cold thermostat is established, as illustrated by the asymptotic behavior of the energy current.

Our calculations confirmed that a brute force evaluation of the currents at the level of accuracy necessary to determine the transport coefficients requires a number of D-NEMD trajectories that is too large for practical purposes. In particular, the single species mass currents showed fluctuations too large to distinguish the signal from the noise with the employed ensemble of 2000 trajectories. To circumvent this problem, we have used a time averaging procedure that smooths out the high frequency fluctuations in the signal coming from each D-NEMD trajectory. From the smoothed results, a clear picture could be extracted for all currents.

Acknowledgement

To Keith, first magister admired from afar, then close friend and highly respected colleague. We see each other only once in a Blue Moon but always with great pleasure, greatly enhanced by Pauline's friendship.

The authors acknowledge support from the CINECA - Italian SuperComputing Resource Allocation (ISCRA) through the PydNEMD-HP10CBZWQK grant.

References

(1) Gubbins, K. E. In *Statistical Mechanics: Volume 1*; Singer, K., Ed.; The Royal Society of Chemistry, 1973; Vol. 1; pp 194–253.

(2) Ludwig, C. Diffusion zwischen ungleich erwwärmten Orten gleich zusammengestzter Lösungen. *Sitz. Ber. Akad. Wiss. Wien Math-Naturw. Kl.* **1856**, *20*, 539.

(3) Soret, C. Influence de la température sur la distribution des sels dans leurs solutions. *C. R. Acad. Sci.* **1880**, *91*, 289.

(4) Reith, D. M.; Müller-Plathe, F. On the nature of thermal diffusion in binary Lennard-Jones liquids. *J. Chem. Phys.* **2000**, *112*, 2436–2443.

(5) Longree, D.; Legros, J. C.; Thomaes, G. Measured Soret Coefficients for Simple Liquified Gas Mixtures at Low Temperatures. *J. Phys. Chem.* **1980**, *84*, 3480–3483.

(6) Platten, J. K. The Soret effect: A review of recent experimental results. *J. Appl. Mech.* **2006**, *73*, 5–15.

(7) Köhler, W.; Morozov, K. The Soret Effect in Liquid Mixtures – A Review. *Journal of Non-Equilibrium Thermodynamics* **2017**, *41*, 151–197.

(8) Köhler, W.; Rossmanith, P. A new holographic grating technique for the measurement of diffusion and thermal diffusion of polymers in solution. *Int. J. Polym. Anal. Charact.* **1995**, *1*, 49–62.

(9) Vogelsang, R.; Hoheisel, C. Thermal conductivity of a binary-liquid mixture studied by molecular dynamics with use of Lennard- Jones potentials. *Phys. Rev. A* **1987**, *35*, 3487–3491.

(10) Paolini, G. V.; Ciccotti, G. Cross thermotransport in liquid mixtures by nonequilibrium molecular dynamics. *Phys. Rev. A* **1987**, *35*, 5156–5166.

(11) Sarman, S.; Evans, D. J. Heat Flow and mass difFusion in binary Lennard-Jones mixtures. *Phys. Rev. A* **1992**, *45*, 2370–2379.

(12) Hafskjold, B.; Ikeshoji, T. Non-equilibrium molecular dynamics calculation of heat conduction in liquid and through liquid-gas interface. *Mol. Phys.* **1994**, *81*, 251–261.

(13) Perronace, A.; Ciccotti, G.; Leroy, F.; Fuchs, A.; Rousseau, B. Soret coefficient for liquid argon-krypton mixtures via equilibrium and nonequilibrium molecular dynamics: A comparison with experiments. *Phys. Rev. E* **2002**, *66*, 031201.

(14) Galliéro, G.; Duguay, B.; Caltagirone, J.-P.; Montel, F. On thermal diffusion in binary and ternary Lennard-Jones mixtures by non-equilibrium molecular dynamics. *Philos. Mag.* **2003**, *83*, 2097–2108.

(15) Galamba, N.; de Castro, C. A. N.; Ely, J. F. Equilibrium and nonequilibrium molecular dynamics simulations of the thermal conductivity of molten alkali halides. *J. Chem. Phys.* **2007**, *126*, 204511.

(16) Bugel, M.; Galliero, G. Thermal conductivity of the Lennard-Jones fluid: An empirical correlation. *Chem. Phys.* **2008**, *352*, 249–257.

(17) Artola, P.-A.; Rousseau, B. Thermal diffusion in simple liquid mixtures: what have we learnt from molecular dynamics simulations? *Molecular Physics* **2013**, *111*, 3394–3403.

(18) Ishii, Y.; Sato, K.; Salanne, M.; Madden, P. A.; Ohtori, N. Thermal conductivity of molten alkali metal fluorides (LiF, NaF, KF) and their mixtures. *J. Phys. Chem. B* **2014**, *118*, 3385–3391.

(19) Pourali, M.; Maghari, A. Non-equilibrium molecular dynamics simulation of thermal conductivity and thermal diffusion of binary mixtures confined in a nanochannel. *Chem. Phys.* **2014**, *444*, 30 – 38.

(20) Ferrario, M.; Bonella, S.; Ciccotti, G. On the establishment of thermal diffusion in binary Lennard-Jones liquids. *Eur. Phys. J.: Spec. Top.* **2016**, *225*, 1629–1642.

(21) Galliero, G. et al. Thermodiffusion in multicomponent n-alkane mixtures. *npj Microgravity* **2017**, *3*, 20.

(22) Ciccotti, G.; Jacucci, G. Direct computation of dynamical response by molecular dynamics: The mobility of a charged Lennard-Jones particle. *Phys. Rev. Lett.* **1975**, *35*, 789–792.

(23) Onsager, L. Reciprocal relations in irreversible processes. I. *Phys. Rev.* **1931**, *37*, 405–426.

(24) Onsager, L. Reciprocal relations in irreversible processes. II. *Phys. Rev.* **1931**, *38*, 2265–2279.

(25) Trimble, R.; Deutch, J. Molecular derivation of the hydrodynamic equations for a binary fluid. *J. Stat. Phys.* **1971**, *3*, 149–169.

(26) Sindzingre, P.; Ciccotti, G.; Massobrio, C.; Frenkel, D. Partial enthalpies and related quantities in mixtures from computer simulation. *Chem. Phys. Lett.* **1987**, *136*, 35–41.

(27) Sindzingre, P.; Massobrio, C.; Ciccotti, G.; Frenkel, D. Calculation of partial enthalpies of an argon-krypton mixture by NPT molecular dynamics. *Chem. Phys.* **1989**, *129*, 213–224.

(28) Ciccotti, G.; Jacucci, G.; McDonald, I. R. Transport properties of molten alkali halides. *Phys. Rev. A* **1976**, *13*, 426–436.

(29) Ciccotti, G.; Jacucci, G.; McDonald, I. R. Thermal response to a weak external field. *J. Phys. C: Solid State Phys.* **1978**, *11*, L509–L513.

(30) Ciccotti, G.; Kapral, R.; Sergi, A. In *Handbook of Materials Modeling. Volume I: Methods and Model*; Yip, S., Ed.; Springer, Berlin, 2005; pp 1–17.

(31) Mugnai, M. L.; Caprara, S.; Ciccotti, G.; Pierleoni, C.; Mareschal, M. Transient hydrodynamical behavior by dynamical nonequilibrium molecular dynamics: The formation of convective cells. *J. Chem. Phys.* **2005**, *131*, 064106.

(32) Orlandini, S.; Meloni, S.; Ciccotti, G. Hydrodynamics from statistical mechanics: Combined dynamical-NEMD and conditional sampling to relax an interface between two immiscible liquids. *Phys. Chem. Chem. Phys.* **2011**, *13*, 13177–13181.

(33) Pourali, M.; Meloni, S.; Magaletti, F.; Maghari, A.; Casciola, C. M.; Ciccotti, G. Relaxation of a steep density gradient in a simple fluid: Comparison between atomistic and continuum modeling. *J. Chem. Phys.* **2014**, *141*, 154107.

(34) Ciccotti, G.; Ferrario, M. Dynamical non-equilibrium molecular dynamics. *Entropy* **2014**, *16*, 233–257.

(35) Ciccotti, G.; Ferrario, M. Non-equilibrium by molecular dynamics: a dynamical approach. *Mol. Simul.* **2016**, *42*, 1385–1400.

(36) Ciccotti, G. In *Computer Simulation in Material Science*; Meyer, M., Pontikis, V., Eds.; NATO ASI Series E, Applied Sciences, 1991; pp 119–137.

(37) Ciccotti, G.; Pierleoni, C.; Ryckaert, J. P. In *Microscopic Simulations of Complex Hydrodynamic Phenomena*; Mareschal, M., Holian, B. L., Eds.; Plenum Press, New York, 1992; pp 25–45.

(38) Irwing, J.; Kirkwood, J. The statistical mechanical theory of transport processes. IV. The equations of hydrodynamics. *J. Chem. Phys.* **1950**, *18*, 817–829.

(39) Allen, M. P.; Tildesley, D. J. *Computer Simulation of Liquids*; Clarendon Press, Oxford, 1987.

(40) Mountain, R. D. System size and control parameter effects in reverse perturbation

nonequilibrium molecular dynamics. *The Journal of Chemical Physics* **2006**, *124*, 104109.

(41) Wirnsberger, P.; Frenkel, D.; Dellago, C. An enhanced version of the heat exchange algorithm with excellent energy conservation properties. *J. Chem. Phys.* **2015**, *143*, 124104.

(42) Bryk, T.; Mryglod, I. Longitudinal dynamics in a Lennard-Jones binary liquid: Crossover from hydrodynamics to the molecular regime. *Condensed Matter Physics* **2004**, *7*, 15–34.

(43) Mikhailenko, S. A.; Dudar, B. G.; Derkach, V. N.; Zozulya, V. N. Volume and shear viscosities of liquid argon-krypton mixtures. *Soviet Journal of Low Temperature Physics* **1977**, *3*, 685–694.

Graphical TOC Entry